A&A manuscript no.
(will be inserted by hand later)

Your thesaurus codes are:
07(02.08.1;02.18.7;08.03.1;08.03.4;08.12.1)

ASTRONOMY
AND
ASTROPHYSICS
4.4.1995

Circumstellar dust shells around long-period variables

IV. Brightness profiles and spatial spectra of C-stars

J.M. Winters[1], A.J. Fleischer[1], A. Gauger[1,2], and E. Sedlmayr[1]

[1] Technische Universität Berlin, Institut für Astronomie und Astrophysik, Sekr. PN 8-1, Hardenbergstr. 36, D–10623 Berlin, Federal Republic of Germany

[2] Los Alamos National Laboratory, Group T-4, MS B268, Los Alamos, NM 87545, USA

Received ; accepted

Abstract. Theoretical brightness profiles and spatial spectra of dynamical models for circumstellar dust shells of long–period variables are presented.

Based on dynamical models of circumstellar dust shells, which include time–dependent hydrodynamics and a detailed treatment of the processes of formation, growth and evaporation of carbon grains, frequency–dependent radiative transfer calculations have been carried out which yield the synthetic brightness distributions and spatial spectra of these dust shell models.

The brightness profiles show a pronounced time–dependent internal structure on a spatial scale of a few stellar radii, which reflects the discrete shell–like distribution of dust across the circumstellar shell. Internal structures are also present in the synthetic spatial spectra (or visibilities) calculated from these intensity profiles. Similar structures, which are present in the observed brightness profiles and spatial spectra of several long–period variable stars can be physically explained by the formation of discrete dust layers resulting from the model calculations presented here. We also find temporal variations of the synthetic spatial spectra which are in quantitative agreement with respective observations. Our model calculations indicate, that the instants of time, when the minimum and maximum value of the visibility is reached depend on wavelength.

Key words: hydrodynamics – radiative transfer – stars: carbon – circumstellar matter – stars: late–type

Send offprint requests to: J.M. Winters
e-mail: `Winters@physik.TU-Berlin.DE`

1. Introduction

A common feature of late–type stars evolving along the Asymptotic Giant Branch (AGB) is the occurrence of stellar pulsation with typical periods of approximately 1 yr accompanied by the formation of spatially extended, expanding circumstellar dust shells (CDS) (e.g. Jura 1986). In order to explain the slow, massive winds ($5\,\mathrm{km\,s^{-1}} < v_\infty < 35\,\mathrm{km\,s^{-1}}$, $3\,10^{-7} M_\odot \mathrm{yr}^{-1} < \dot{M} < 5\,10^{-5} M_\odot\,\mathrm{yr}^{-1}$, e.g. Loup et al. 1993) of these long–period variable stars (LPVs), a two–step mechanism has been proposed as being responsible for the mass–loss of these objects (Jones et al. 1981): i) levitation of the atmosphere by dissipation of shock waves generated by the interior pulsation of the star, and ii) acceleration of the material by radiation pressure on dust, which condenses in the region of sufficiently enhanced density.

Although other single driving mechanisms have also been discussed in the literature (e.g. driving by acoustic waves (Pijpers & Habing 1989), Alfvén waves (Holzer et al. 1983), or radiation pressure on dust (e.g. Tielens 1983, Gail & Sedlmayr 1987)), a two–step process involving the dissipation of shock wave momentum seems to be the most promising mechanism in the case of pulsating late–type stars. Already Wood (1979) had to introduce an additional acceleration term (simulating radiation pressure on dust) into his pulsation models, since the shock waves alone were not able to explain both, the observed high mass loss rates and the low outflow velocities at once. This approach has been improved by Bowen (1988) and Fleischer et al. (1992, henceforth called Paper I), who confirmed the decisive role of radiation pressure on dust to produce the slow, massive winds of LPVs.

Several investigations have been carried out from the observational side which were aimed at exploring the location and spatial distribution of the dust around pulsating late–type stars. Since these objects are intrinsically cool ($T_\star < 3000\,\mathrm{K}$, e.g. Olofsson et al. 1993b) and the dust grains additionally redistribute the absorbed radiation energy at longer wavelengths after an internal relaxation process, these observations are mainly performed in the infrared spectral region. From fitting the observed energy distributions of several carbon–rich LPVs as a function of phase of the lightcurve, Le Bertre (1988b, 1988a) concluded that dust formation takes place at around $6R_\star$ and that the location of dust formation varies with time in these objects. A similar conclusion was drawn by Ridgway & Keady (1988) and Danchi et al. (1990) from interferometric observations of IRC +10216 and, more recently, by Danchi et al. (1994) for several additional oxygen–rich LPVs. In this work, the inner radii of the dust shells are found to be located at a distance of about 2–$7R_\star$ above the photosphere for 7 objects out of a total of 13 objects contained in the sample of Danchi et al. (1994).

In order to fit the observed energy distributions and the spatial spectra, usually rather simple models, which implicitly assume a stationary outflow, are used to describe the radial distribution of dust across the circumstellar shell (e.g. Rowan–Robinson & Harris (1983), Martin & Rogers (1987), Le Bertre (1988b), Danchi et al. (1994)). These models however do not account for the detailed physical processes taking place in the atmosphere, e.g. for the interaction between stellar pulsation and the dust formation process. Also, in order to analyze the measured spatial spectra and to derive the angular size of the radiation emitting region of the dust shell, simple assumptions about the object's brightness distribution are made, e.g. a Gaussian intensity distribution is frequently assumed for simplicity (cf. Dyck et al. 1984). Of course, these methods allow to get a general picture of global characteristics of the shells (e.g. the approximate distance of the inner edge of the dust shell from the star and of the typical temperature in this region) but these models are by no means unique and, of course, cannot provide reliable detailed information about the real spatial structure of the shell and the physical processes which determine this structure.

Recent theoretical modelling of the CDS of carbon–rich LPVs revealed a complex dynamical interplay between the interior pulsation of the star and the process of dust formation in the circumstellar shell (Fleischer et al. 1992, 1995, Höfner et al. 1995). Caused by the nonlinear coupling between stellar pulsation and the dust complex the radial stratification of the dust shell models shows a rather complex onion–like dust distribution, which decisively influences the hydrodynamical and thermodynamical structure throughout the CDS. This shell–like structure of the CDS is caused by the periodic formation of new dust layers in the inner region of the CDS. It was shown in Winters et al. (1994b, henceforth called Paper II), that the periodic formation of a new dust layer strongly influences the synthetic lightcurves resulting from these models. In the present paper, we investigate some general implications of the discrete radial structure of these dust shell models on the synthetic brightness profiles and the corresponding spatial spectra.

We start with a short description of the modelling method in Sect. 2. The results are given in Sect. 3 and are followed by a discussion in section 4 where we qualitatively compare our exemplary calculations with corresponding results from observations. We finish this paper with the conclusions in Sect. 5.

2. The modelling method

The details of our modelling method and the basic equations have been discussed elsewhere (Paper I, Winters et al. 1994a), therefore we only give a brief summary of the main ingredients here.

2.1. Hydrodynamical model calculation

We consider a spherically symmetric atmosphere surrounding a pulsating red giant, characterized by its mass $M_\star$, effective temperature $T_\star$, luminosity $L_\star$, pulsation period P, and the photospheric element abundances ϵ_i.

The time–dependent hydrodynamical equations are discretized in Lagrangian coordinates and solved by explicit integration in time according to the difference scheme given in Richtmyer & Morton (1967). Cooling of the gas behind the shock fronts is assumed to take place instantaneously, i.e. we treat the shocks in the isothermal limit case. If cooling of the post–shock gas is taken into account, the interaction processes become more complicated but the discrete structure of the CDS is conserved (Gauger et al. 1994). Since the main cause for the behaviour of the radial brightness distributions (see Sect. 3) is the periodic formation of dust, the results presented here do also appear in models where time–dependent post–shock cooling of the gas is taken into account (cf. Winters et al. 1995).

The process of dust nucleation is treated in the framework of classical nucleation theory as summarized in Gail et al. (1984), growth and thermal evaporation of the dust grains is described by the set of moment equations developed by Gail & Sedlmayr (1988) and Gauger et al. (1990). For the calculation of the dust complex it is essential to know the chemical composition of the gas phase. We use a set of the relevant hydrocarbons (H, H_2, C, C_2, C_2H, C_2H_2) in chemical equilibrium to calculate the particle densities of the species contributing to the growth of carbon grains. Solar abundances (Allen 1973) are assumed for all elements except for the abundance of carbon ϵ_C which we consider as a free model parameter in order to account for a carbon–rich element composition.

For the calculation of the dynamical structure of the circumstellar shell the radiative transfer problem is treated by the grey Eddington approximation in spherical geometry (Lucy 1971, 1976) which yields the local equilibrium temperature T_{eq} at every instant of time. Since we assume isothermal shocks, the gas temperature T_g equals T_{eq} throughout the atmosphere at every instant of time.

Furthermore, the dust grains are assumed to be completely momentum coupled to the ambient gas. This assumption is justified, if the mass loss rate exceeds a lower limit value of about $10^{-8} M_{\odot} \mathrm{yr}^{-1}$ (e.g. MacGregor & Stencel (1992), Krüger et al. (1994)), which is the case for the models presented here (cf. Tab. 1). However, the particles are not necessarily position coupled to the gas, but are moving with their size–dependent drift velocity relative to the gas. Since the mean particle radius of the dust grains is smaller than 0.1μm throughout the dust shell in all calculations presented here, the drift velocity of the dust grains is of the order of the thermal velocity of the gas, which is small compared to the expansion velocity (cf. the estimate given in Sect. 4.2 of Paper I and the more thorough investigation of Krüger et al. (1994)). The neglect of drift, therefore, is a reasonable approximation for the models discussed in this paper.

At the inner boundary of the model a sinusoidal variation of the velocity with amplitude Δu and period P is applied to simulate the interior pulsation of the star.

Thus, our models are defined by the prescription of the 4 fundamental stellar parameters ($T_\star$, $L_\star$, $M_\star$, $\epsilon_{\rm i}$) and of (P, Δu) to describe the interior pulsation. To start the calculation, an initial hydrostatic model with the chosen number of grid points (here 1024) and the desired values of $T_\star$, $L_\star$ and $M_\star$ is constructed. The velocity amplitude of the piston is increased slowly until the maximum value Δu is reached and the calculation of the dust complex, which requires the specification of $\epsilon_{\rm i}$, is started simultaneously. The development of the model is followed in time until a regular pattern of the radial structure is reached.

2.2. Radiative transfer calculation

For a given radial structure of the dust shell model, i.e. at a fixed instant of time, we solve the frequency–dependent stationary radiative transfer equation in spherical geometry. The radiation field is calculated by a Feautrier type iteration between the monochromatic moment equations (the system is closed by the variable Eddington factor) and the formal solution for the monochromatic specific intensity along the characteristic lines of the partial differential equation. Details of this method are given in Winters (1994).

The radiative transfer processes considered are grey absorption and thermal emission of the gas and frequency–dependent absorption and thermal emission of the dust component. The gas opacity is approximated by a constant value of $\kappa^{\rm g}/\rho = 2\,10^{-4} \mathrm{cm}^2\mathrm{g}^{-1}$ (ρ: mass density) (cf. Bowen 1988, Paper I), which roughly represents the Rosseland mean gas opacity in the relevant temperature and density range. For calculating the dust opacity the dust particles are assumed to be spherical and small compared to the relevant wavelengths of the radiation field. The assumption of the *small particle limit* is approximately justified for the time–dependent models considered here, since the mean particle radius remains smaller than 0.1μm throughout the circumstellar shell (cf. Paper I, Fleischer 1994). With these assumptions the absorption coefficient of the dust component $\kappa_\nu^{\rm d}$ is expressed by (cf. Gail et al. 1984)

$$\kappa_\nu^{\rm d}(r) = \frac{8\pi^2 a_0^3}{\lambda} \mathrm{Im}\left\{\frac{m(\nu)^2-1}{m(\nu)^2+2}\right\} K_3(r) = \chi_\nu^{\rm d}(r)\,, \tag{1}$$

and equals the extinction coefficient of the dust component $\chi_\nu^{\rm d}$. For all calculations presented here, the complex refractive index $m(\nu)$ of the grain material is taken from Maron (1990) which is appropriate for pure amorphous carbon grains and gives roughly a λ^{-1} dependence of the extinction coefficient. The quantity $K_3(r)$ is the third moment of the size distribution function $f(a,r)$ of the dust particles, representing the number of monomers condensed into grains. It is defined by

$$a_0^3 K_3 = \int_{a_\ell}^{\infty} a^3 f(a,r) da\,, \tag{2}$$

where a is the radius of the dust grain, a_0 denotes the hypothetical radius of a monomer contained in a dust grain ($a_0 = 1.28\,10^{-8}$ cm in the case of pure carbon grains), and a_ℓ is a lower limit size of the dust particles ($a_\ell \approx 10^{-7}$cm). Since we assume the dust particles to be small compared to the wavelength, we neglect the contribution of light scattering by the grains. Thus, the emissivity ϵ_ν is given by thermal emission of gas and dust:

$$\epsilon_\nu(r) = \epsilon_\nu^{\rm g}(r) + \epsilon_\nu^{\rm d}(r) = \left(\kappa^{\rm g}(r) + \kappa_\nu^{\rm d}(r)\right)\, B_\nu\left(T(r)\right)\,, \tag{3}$$

where B_ν is the Kirchhoff–Planck function and the superscripts $^{\rm g}$ and $^{\rm d}$ denote the gas and the dust component, respectively.

By definition, K_3 equals the number of monomers condensed into grains per cm^3 and, therefore, is related to the degree of condensation f_c, i.e. the fraction of condensable material actually condensed into grains. In the case of pure carbon grains, which is considered here, the degree of condensation is given by

$$f_c = \frac{K_3}{(\epsilon_{\rm C} - \epsilon_{\rm O}) n_{<\rm H>}}\,, \tag{4}$$

where we have assumed that all oxygen is locked up in the CO–molecule ($n_{<\rm H>}$: total density of hydrogen nuclei). Thus, the radiative acceleration in units of the local gravitational deceleration

$$\alpha = \frac{\chi_H}{\rho} \frac{L_\star}{4\pi c G M_\star} \tag{5}$$

is directly proportional to the degree of condensation (χ_H: flux–mean extinction coefficient, c: speed of light, G: gravitational constant).

Table 1. Parameters of the initial hydrostatic models. Also given are the stellar radii of the initial models and the time averaged mass loss rates and final outflow velocities of the evolved models.

	Model A	Model B	Model C
$M_\star$ [$M_\odot$]	1.0	1.0	1.0
$L_\star$ [$10^4\ L_\odot$]	1.0	1.0	0.9
$T_\star$ [K]	2600	2500	2500
ϵ_C/ϵ_O	1.8	1.34	1.60
P [d]	650	370	388
Δu [km s^{-1}]	2.0	6.0	3.0
R_0 [10^{13} cm]	3.43	3.70	3.51
$<\dot{M}>$ [$M_\odot$ yr^{-1}]	1.0 10^{-5}	3.0 10^{-5}	2.2 10^{-5}
$<u_\infty>$ [km s^{-1}]	28.5	12.8	21.7

3. Results

Table 1 summarizes the parameters of the three models discussed here. Additionally given are the time averaged values of the mass loss rate and the final outflow velocity of the evolved models. Models A and B are the same as in Paper II, while Model C is different. We have chosen the model parameters to represent typical cool, dust–enshrouded carbon giants. For these objects, e.g. Claussen et al. (1987) find typical values of the luminosity of the order of $10^4 L_\odot$, irrespective of the pulsation period. The investigations of Lambert et al. (1986) and Olofsson et al. (1993a, 1993b) show, that the objects under consideration are in fact rather cool with effective temperatures well below or approximately 3000 K. Lambert et al. (1986) find values of the C/O–ratio up to 1.76, whereas Frantsman & Eglitis (1988) report on a considerable fraction of stars having C/O$>$ 2. The typical periods found for C–rich LPVs range from less than 300d up to more than 700d (cf. Olofsson et al. (1993a), Le Bertre (1992)).

Although the values of the model parameters were chosen from different observational investigations, they do not contradict the well known core mass–luminosity relations obtained from the results of stellar evolution calculations (e.g. Boothroyd & Sackmann 1988). Furthermore, the resulting quantities, e.g. the mass loss rates and terminal wind velocities, lie well within the range observed for carbon–rich LPVs (cf. Olofsson et al. (1993a) and Loup et al. (1993))

3.1. Radial structure of the dust shell models

Figure 1 depicts the typical radial structure of the CDS at different instants of time (corresponding to the instants shown in Figs. 3a), 4a), and 5a)) for Models A, B, and C (cf. Tab. 1). The beginning of the hydrodynamical cycle (i.e. $t = 0\,P$) is defined by the motion of the inner boundary which is moving outwards with maximum velocity Δu at this instant. The following quantities are plotted:

upper row: the velocity v (solid line) and the degree of condensation f_c, i.e. the fraction of condensable material actually condensed into grains (dashed line) (cf. Eq. (4)),

lower row: the logarithm of the third moment of the particle size distribution function K_3 (solid line) (cf. Eq. 2, K_3 is proportional to the product $\rho \cdot f_c$) and the temperature T (dashed line).

Radii are always given in units of the stellar radius R_0 of the initial hydrostatic model.

The consistent calculation of dust condensation, grain growth, and grain destruction turns out to have significant influence on the resulting dynamical structure of the CDS. As the degree of condensation f_c in Fig. 1 shows, the dust is distributed inhomogeneously across the shell. The dust grains are concentrated in distinct layers and exhibit a shell or onion–like structure which is closely related to the velocity structure of the CDS.

Fig. 1 also shows the influence of the dust on the thermodynamical structure of the CDS. There are steps in the course of the temperature stratification which coincide with peaks in the amount of condensed material.

These interactions have been investigated in detail in Paper I and, therefore, are only briefly summarized here.

The discrete structure of the atmosphere is not produced solely by the shock waves caused by the interior pulsation of the star, but is a very product of the process of dust formation. In a first step the interior pulsation defines the onset of dust *nucleation* by providing appropriate low temperatures in the region around $3R_0$. In a second step, pulsation triggers grain *growth* by a compression of the material in this region, thereby providing the high densities favourable for the growth process. In a short time interval values of f_c as high as 1 are reached within the new dust layer, i.e. all condensable material is actually condensed into grains. The quantity f_c is proportional to the radiative acceleration of the dust grains (cf. Paper I and Eqs. (1), (4), (5)). Due to close momentum coupling of the grains to the ambient gas, the sudden increase of the radiative acceleration causes a perturbation in the velocity field which steepens to become a shock wave, thereby compresses the material and, in turn, accelerates dust growth. Thus, the prominent shock waves which propagate through the atmosphere (cf. Fig. 1) are produced by a self–accelerating mechanism caused by dust formation.

Furthermore, the newly formed dust in the inner shells, due to its opacity, effectively blocks the outgoing radiation and heats the material closer to the star. This back–warming, seen as steps in the temperature structure in

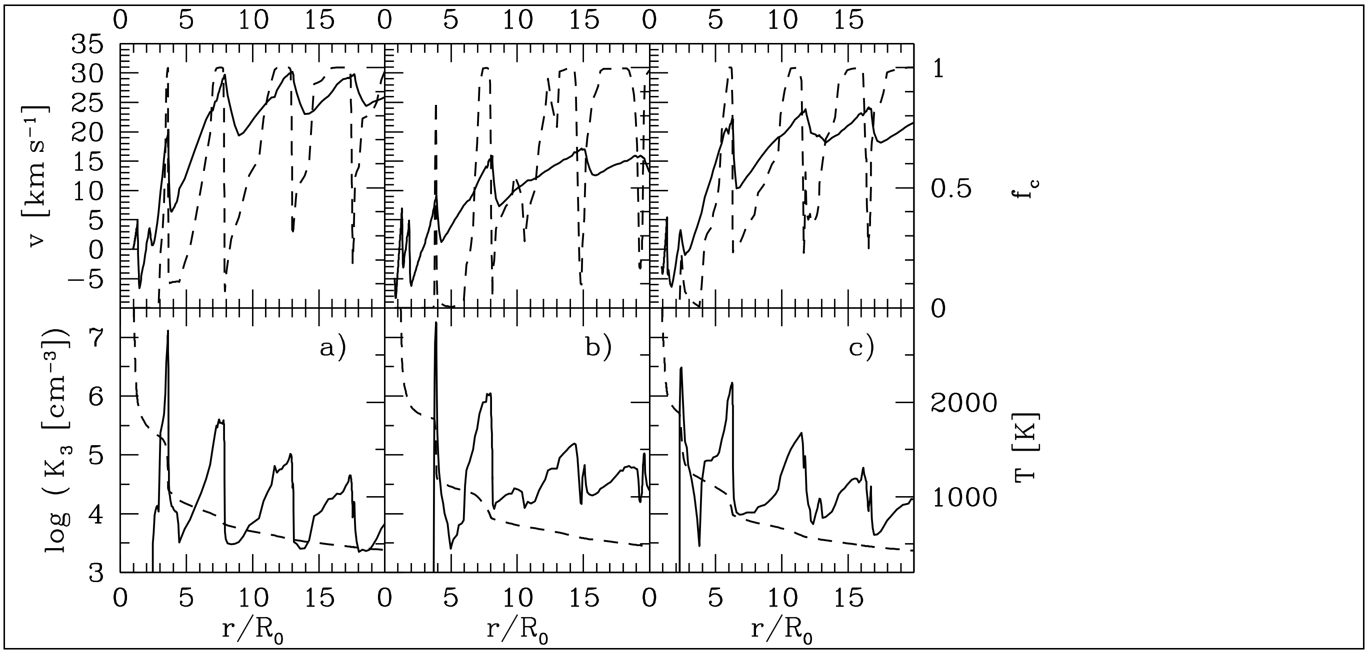

Fig. 1. Radial structure of: **a)** Model A at $t = 0.25P$, **b)** Model B at $t = 0.60P$, and **c)** Model C at $t = 0.55P$

Fig. 1, in turn limits the condensation of new dust particles.

Due to pulsation and back–warming, dust formation and growth is only possible in a small radius range and during a limited time interval. This results in the discrete structure of the CDS. The complex interplay among the processes of dust formation and growth, hydrodynamics and thermodynamics shows that the dust particles play a key role in determining the atmospheric structure of LPVs.

3.2. Temporal behaviour of the models

In the case of Model A, *every* hydrodynamic period a new dust layer is formed in the region between $2R_0$ and $4R_0$, whereas the same occurs in Model B only every 4^{th} pulsation cycle. In Model C, a new dust layer is formed approximately every three pulsation cycles, but the details of the dust formation process are not repeated exactly after this time interval (cf. Fig. 2). Thus, the atmospheric structure of Model A is periodic on a timescale of one pulsation period, Model B exhibits the effect of *multiperiodicity* with a multiperiodicity number $n_{\rm P} = 4$ (cf. Fleischer 1994) and the structure of Model C is slightly irregular. This different temporal behavior of the three models is caused by a nonlinear interaction between the interior pulsation of the star (simulated by a sinusodially moving inner boundary, cf. Sect. 2.1) and the *exterior* κ*–mechanism*, discussed in Fleischer et al. (1995) and Höfner et al. (1995). A detailed analysis of the effect of multiperiodicity is beyond the scope of the present work and will be given in a forthcoming paper of this series.

Independent of the (multi–)periodic behavior of the models, each newly formed dust layer subsequently moves outwards, thereby producing a more (Models A and B) or less (Model C) regular pattern of the layered distribution of dust across the CDS. As was demonstrated in Paper II, the periodic formation of new dust layers leads to pronounced effects, e.g. to intermediate maxima, in the synthetic lightcurves or to multiperiodic lightcurves, which compare well to similar structures already observed in the lightcurves of real LPVs.

Figure 2 depicts the synthetic lightcurves at two different wavelengths and the temporal behaviour of the dust optical depth $\tau^{\rm d}$ at $\lambda = 1\mu$m for Models A, B, and C. From the lower row of Fig. 2 it can be seen, that the formation of a new dust layer in the inner shell region leads to a steep increase of the optical depth within an interval of about 10% of the pulsation period. The formation of a new dust layer takes place around $t = 0.70P$ for Model A, around $t = 3.5P$ for Model B, and e.g. around $t = 3\,P$ for Model C. In all three models, the phase of dust formation coincides with the phase of light minimum (for Models B and C these are the deep minima), cf. the lightcurves shown in the 1^{st} and 2^{nd} row of Fig. 2. In the *multiperiodic* Models B and C, $\tau^{\rm d}$ additionally exhibits an alternating behaviour during the time interval between the formation of successive layers (see lower row of Fig. 2). These intermediate variations of the optical depth are a consequence of the periodically enhanced density in the dust formation region caused by the shock waves: The passage of subsequent shocks (following the formation of a new dust layer) almost periodically enhances the gas density at the

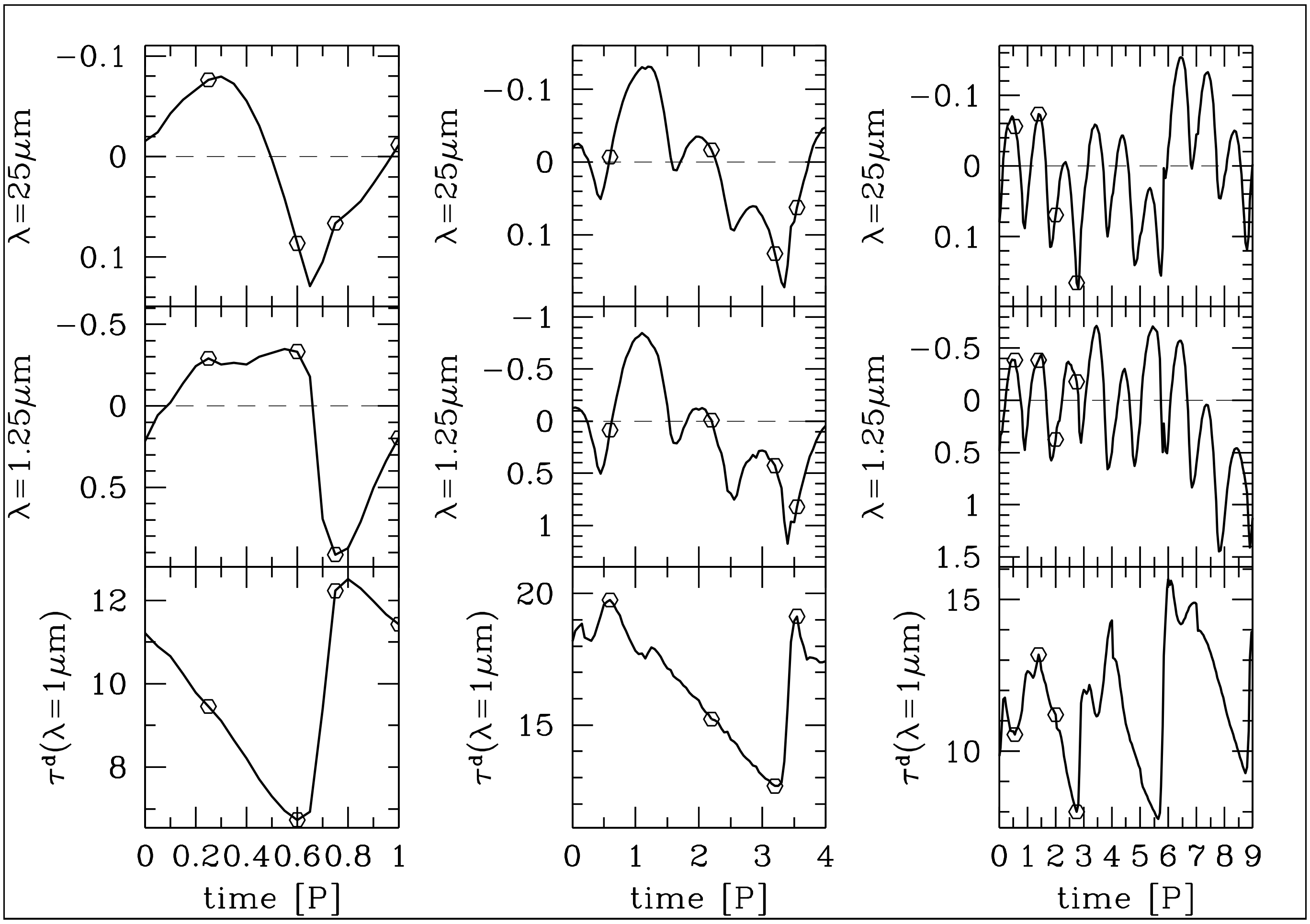

Fig. 2. Temporal variation of several quantities for Model A over one pulsational period (left hand column), for Model B over four pulsational periods (middle column), and for Model C over nine pulsational periods (right hand column). For each Model, the following quantities are plotted:
1st row: lightcurve at 25μm in magnitudes, normalized to the mean value
2nd row: lightcurve at 1.25μm in magnitudes, normalized to the mean value
3rd row: dust optical depth $\tau^{\rm d}$ at $\lambda = 1\mu$m.
Open hexagons indicate the instants of time, at which the spatial structure of the models is shown in Sect. 3.3.

position of the newly formed dust layer. This provides favorable conditions for a further *growth* of the already existing dust particles and, therefore, to a corresponding increase of the degree of condensation. Since the extinction coefficient of the dust component is proportional to f_c (cf. Eqs. (1) and (4)), the optical depth increases accordingly. The subsequent phase of decreasing optical depth is caused by the geometrical dilution in particular of the innermost dust layer after the passage of the shock. Once the degree of condensation in the innermost layer has reached a value close to unity, the passage of further shocks merely drives the dust layer outwards, causing the comparably long phase of continuously decreasing optical depth (between $t = 1.5P$ and $t = 3.2P$ for Model B and e.g. between $t = 1.5P$ and $t = 2.7P$ for Model C).

In Paper II it was in particular described, how the intermediate structures in the lightcurves of Model A (cf. left column of Fig. 2) are produced by the formation of a new dust layer. There we suggested, that dust formation might be responsible for similar structures observed in the lightcurves of several carbon–rich LPVs (e.g. AFGL 1062, AFGL 1085, AFGL 1235, R Lep, R Scl, cf. Le Bertre 1992). However, other mechanisms are currently discussed in the literature, which in principle may also explain the intermediate maxima present in the observed lightcurves. These mechanisms comprise the dissipation of shock wave energy in the inner parts of the atmosphere which is transferred to the radiation field (see Feuchtinger et al. 1993) and the formation of secondary shocks in the innermost dust–free region (see Bowen (1990), Willson et al. (1994)). Which of the proposed mechanisms actually is at work has not been finally decided yet. However, an independent check of the results of our theoretical models can in fact be based directly on the striking spatial structure of the dust shells and gives further evidence, that the formation of discrete dust layers indeed occurs in the real CDS.

3.3. Spatial intensity profiles and spatial spectra

Due to thermal dust emission emanating from the discrete layers, the discontinuous dust distribution is reflected in the spatial intensity profiles of the dust shell models. The synthetic radial intensity profiles $I(p)$, the integrated intensity profiles $b(p)$ and the theoretical visibilities $V(q)$ are shown for the Models A, B, and C in the following figures 3, 4, and 5 for different wavelengths and at different phases of the pulsation cycle. In each of these figures the time increases from left to right. The instants of time given in each column correspond to the phases marked in Fig. 2 by open hexagons. In the upper two rows of Figs. 3, 4, and 5, p is the impact parameter, i.e. the perpendicular distance of a line of sight from the center of the star (lower abscissa). In the upper abscissa, this distance is converted to an angle Φ, assuming a distance of 200pc.

In the models presented here, the typical separation between the dust layers is of the order of a few R_0, i.e. some 10^{14} cm. Viewed from a distance of 200 pc (only a few real late–type stars are that close to the sun), this separation between the dust layers corresponds to an angular separation of the order of some 0.01 arcsec, which is not easily directly resolvable by current ground–based infrared telescopes. However, in principle it is possible to obtain direct information about the brightness profile with an angular resolution of the order of one milli–arcsecond from lunar occultation observations. By this method, the one–dimensional brightness profile, i.e. the 2-D intensity pattern integrated over the spatial coordinate perpendicular to the lunar motion, is reconstructed from the occultation lightcurve (Williams (1939), Nather & McCants (1970), Richichi (1989)). In order to provide the corresponding theoretical results of our models, the integrated synthetic brightness profiles are depicted in the second row of Figs. 3, 4, and 5.

Unfortunately, only a rather limited number of LPVs is actually covered by the lunar orbit. Therefore, in most cases one has to derive information on the spatial structure of these objects from interferometric measurements. To allow for a comparison with such observations, in the lower row of Figs. 3, 4, and 5 the synthetic spatial spectra (i.e. the visibilities) of the three dust shell models are additionally shown at the same wavelengths and for the same instants of time as the spatial intensity profiles. For calculating the visibilities, also a distance of $d = 200$ pc has been assumed for all three models.

In general, the visibility V as a function of spatial frequencies u and v is the two–dimensional Fourier transform of the intensity distribution $I(\eta, \zeta)$, where η and ζ are the corresponding coordinates on the celestial sphere. In the special case of a circular symmetric intensity distribution, which is produced by the spherical symmetric models, the visibility is given by the Hankel transform of the intensity (e.g. Bracewell (1965)):

$$V(q) = \int_0^{\Phi_{\max}} I(\Phi)\, \Phi\, J_0(2\pi\Phi q)\, d\Phi \ . \tag{6}$$

Here, q $(= \sqrt{u^2 + v^2})$ is the spatial frequency, Φ the angular separation from the center of the star ($\Phi = p/d$) and J_0 the zeroth–order Bessel function. In the following, the term visibility is used to denote the normalized quantity $V(q)/V(0)$.

Caused by the different optical depths of the dust shell at different wavelengths, the emergent intensity exhibits either a step–like structure (at shorter wavelengths) or even local intermediate maxima (at longer wavelengths), which are located at the projected positions of the discrete dust layers. In the integrated brightness profiles (second row of Figs. 3, 4, and 5) these structures are smeared out (e.g. the intermediate maxima have vanished) but the location of the dust layers can still clearly be seen. The radial distance between successive layers of course depends on the period of the dust formation cycle and on the hydrodynamic velocity at the position of the dust layers. As the dust layers are moving outwards, the location of the pronounced structures in the intensity profiles changes accordingly. Therefore, also the synthetic spatial spectra show a corresponding temporal evolution.

3.3.1. Model A

The instants of time at which the radial intensity distributions and the spatial spectra of Model A are plotted in Fig. 3 are:
a) $t = 0.25P$ (left hand column): all dust layers are completely developed (i.e. the degree of condensation has reached 100% in the innermost layer, cf. Fig. 1) and all layers merely are moving outwards;
b) $t = 0.60P$ (second column): just prior to the formation of a new dust layer, this is the instant of minimum shell optical depth (cf. Fig. 2);
c) $t = 0.75P$ (third column): a new dust layer has formed and the shell optical depth has almost reached its maximum value (cf. Fig. 2), and
d) $t = 1.00P$ (right hand column): the newly formed dust grains are still growing but the optical depth is already decreasing due to expansion of the material.

The intensity profile of Model A at 1.65μm (solid line in the upper row of Fig. 3) almost only reflects the temporal behaviour of the innermost dust layer, whereas the outer layers are nearly invisible at this wavelength in the linear scaling of the intensity profile. Thus, the temporal variation of the compact region emitting at 1.65μm

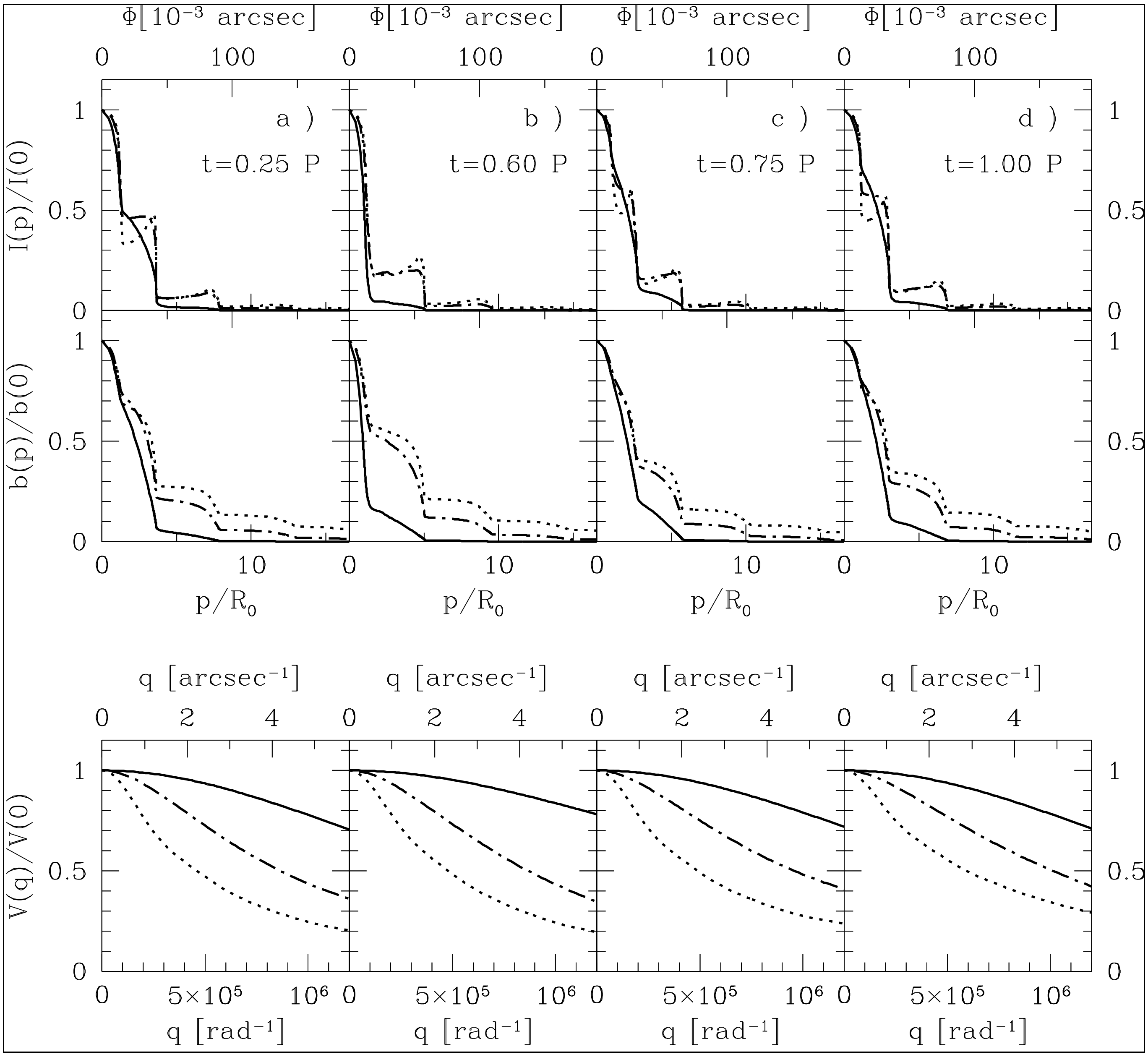

Fig. 3. Intensity profile (upper diagrams), integrated brightness distribution (second row) and visibilities (lower panel) of Model A for $\lambda = 1.65\mu$m (solid lines), $\lambda = 5\mu$m (dash–dotted lines) and $\lambda = 12\mu$m (dotted lines) at different instants of time (see text)

is largely caused by the dynamic evolution of the innermost dust layer. At the longer wavelengths, some of the outer dust layers also contribute to the intensity profile and, even more pronounced, to the integrated brightness profiles (2$^{\rm nd}$ row of Fig. 3). Thermal dust emission from the expanding layers produces steps or even intermediate maxima in the intensity profiles at 5μm and 12μm. The temporal evolution of the intensity distribution leads to a variation of the apparent diameter of the radiation emitting region which is reflected in corresponding changes of the synthetic visibility functions (lower row of Fig. 3). During the pulsation cycle, the temporal variation of the visibility (at a spatial frequency of $q = 10^6\,\mathrm{rad}^{-1}$) amounts to 12% at 1.65μm, 30% at 5μm, and to 66% at 12μm. The minimum visibility (corresponding to maximum apparent extension) is reached for 1.65μm at $t = 0.45P$ and for the other two wavelengths slightly earlier, at $t = 0.40P$.

The visibility maxima occur phase shifted for all wavelengths. At 1.65μm, the maximum visibility (implying minimum extension of the shell region radiating at this wavelength) is reached at $t = 0.65P$, whereas at 5μm the maximum visibility is reached at $t = 0.75P$ and at 12μm at $t = 1.00P$.

The instant of maximum extension at 1.65μm ($t = 0.45P$) occurs after dust growth in the innermost layer has ceased and the layer is already considerably expanded. At 5μm and 12μm, the outer dust layers significantly contribute to the intensity profiles during the whole cycle. At the phase of maximum extension ($t \approx 0.40P$), the front of the dust layer formed in the previous cycle is located around $4.5R_0$ and strongly contributes to the intensity profiles at all three wavelengths.

From the upper diagram of Fig. 3b) it can be seen, that during the phase of minimum extension at 1.65μm (around $t = 0.60P$) almost only the angular region subtended by the stellar surface contributes to the intensity profile at 1.65μm. The maximum visibility (minimum extension) at 5μm and 12μm, which appears at $t = 0.75P$ and $t = 1.00P$, respectively, essentially reflects the current location of the newly formed dust layer at around $3R_0$, although at least the second layer also contributes significantly to the intensity profile. Nevertheless, the minimum extension at the two longer wavelengths might be conceived as a characteristic value for the region, where dust actually forms.

From this result of our model calculations we draw the conclusion that the typical diameters derived from interferometric observations at least of massive circumstellar dust shells depend on wavelength (which is well known) and we also expect that the values derived from such observations for the instants of time, at which the maximum (or minimum) extension is reached, depend on the wavelength.

3.3.2. Model B

For Model B the radial intensity distributions and the spatial spectra are plotted in Fig. 4 at:
a) $t = 0.60P$ (left hand column) at maximum shell optical depth, caused by periodic growth of the innermost dust layer (cf. Fig. 2);
b) $t = 2.20P$ (second column): all dust layers are completely developed and are moving outwards, thereby causing the phase of continuously decreasing optical depth (cf. Fig. 2);
c) $t = 3.20P$ (third column): just prior to the formation of a new dust layer at the instant of minimum optical depth, and
d) $t = 3.55P$ (right hand column): new dust has condensed and the shell optical depth has reached its first intermediate maximum (cf. Fig. 2).

In this multiperiodic model the emitting region is considerably more extended than it is the case in Model A, caused by the much larger contribution of the outer dust layers to the emergent intensity (cf. Fig. 4). Model B has a mass loss rate a factor of three larger than Model A (cf. Tab. 1) and a corresponding higher dust optical depth (cf. Fig. 2). Therefore, a larger amount of thermally emitting dust contributes to the emergent intensity in direction of the line of sight, which results in the more pronounced structures in the intensity profiles. The enhanced contribution of the outer dust layers now leads to the occurrence of a point of inflection in the 5μm visibilities and to pronounced internal structures at longer wavelengths (e.g. at 12μm, see lower row of Fig. 4). In the case of Model A, such structures also occur in the spatial spectra, but only at wavelengths $\lambda > 20\mu$m.

During the dust formation cycle, i.e. an interval of four pulsation periods, the visibility of Model B varies at a spatial frequency of $q = 10^6\,\mathrm{rad}^{-1}$ by 38% at 1.65μm, 34% at 5μm, and by 68% at 12μm. The minimum of the 1.65μm visibility is reached at $t = 1.25P$ while the minimum visibility for the other two wavelengths is reached at $t = 3.35P$. Maximum visibility occurs for 1.65μm at $t = 3.25P$, for 5μm at $t = 0.45P$ and for 12μm at $t = 1.50P$.

Thus, the maximum 1.65μm extension, similar to Model A, occurs when the newly formed layer is almost completely developed, during the phase which is dominated by expansion. The visibilities at 5μm and 12μm indicate maximum extension of the shell when the first maximum of the optical depth is reached after the formation of a new dust layer.

Also similar to Model A, the minimum extension at 1.65μm is reached shortly after the instant of minimum optical depth when the next dust layer begins to form. The visibilities at 5μm and 12μm indicate, that the minimum extensions at these wavelengths occur during the phase of subsequent dust growth in the newly formed layer ($t = 0.45$ for $\lambda = 5\mu$m and $t = 1.50P$ for $\lambda = 12\mu$m).

3.3.3. Model C

Figure 5 depicts the radial intensity distributions and the spatial spectra of Model C at:
a) $t = 0.55P$ (left hand column): intermediate minimum of the shell optical depth (cf. Fig. 2);
b) $t = 1.40P$ (second column): the maximum optical depth during the first dust formation cycle shown in Fig. 2 is reached;
c) $t = 2.00P$ (third column): all dust layers are completely developed and are moving outwards, thereby causing the phase of continuously decreasing optical depth;
d) $t = 2.75P$ (right hand column): just prior to the formation of a new dust layer at the instant of minimum dust optical depth.

Concerning the mass loss rate (cf. Tab. 1), Model C is intermediate between Models A and B. Therefore, the steps in the intensity profiles are less pronounced than in Model B. In contrast to Models A and B, the temporal evolution of the shell structure in this model is slightly irregular on a timescale of approximately three pulsational periods (cf. Fig. 2). The different temporal behavior of the three models is essentially due to the different carbon

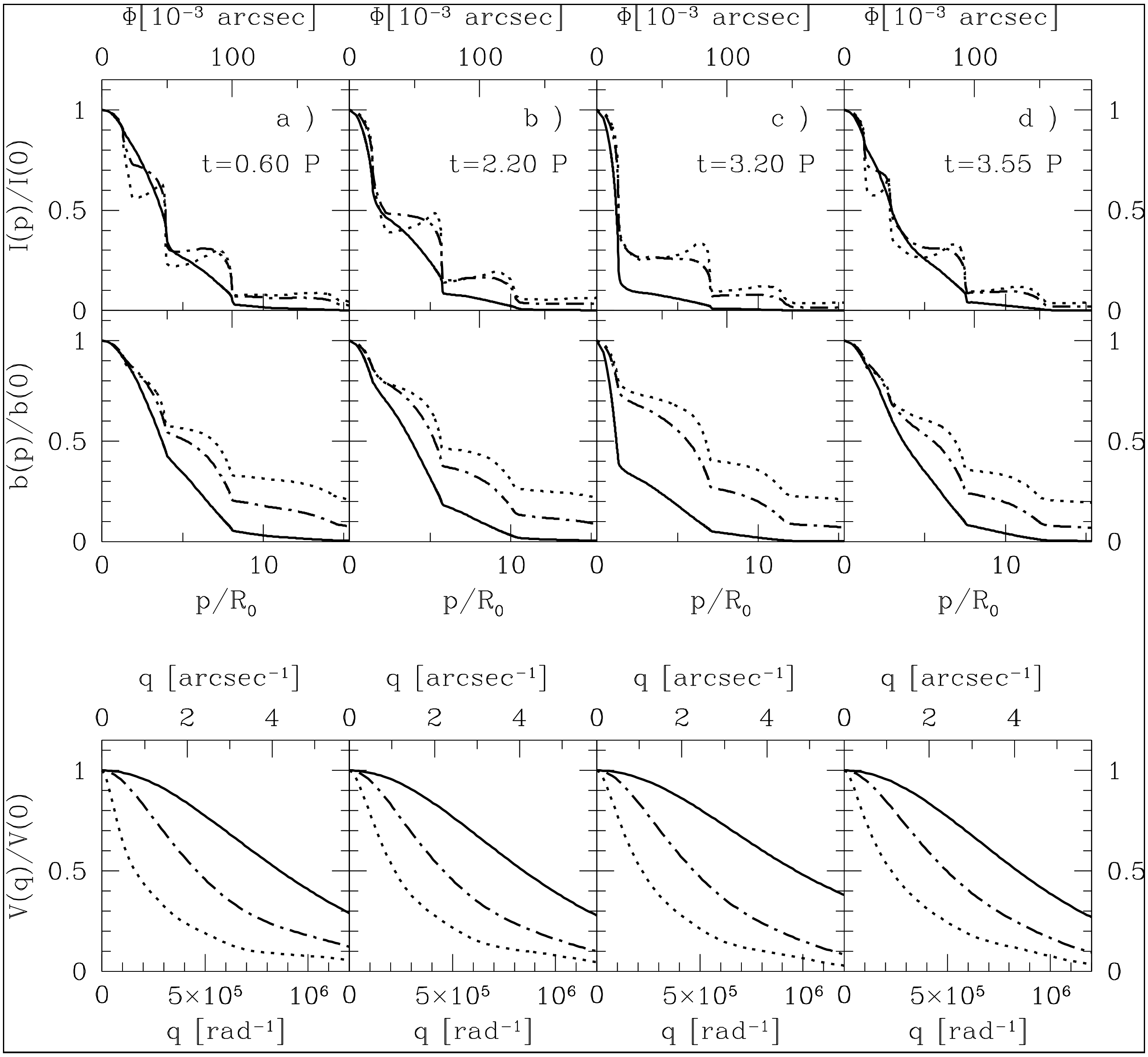

Fig. 4. Same as Fig. 3, but for Model B

abundances assumed for the calculations, whereas it does not depend on the mass loss rate, which is almost independent of ϵ_C. The 12μm visibilities of Model C exhibit a "rippled" structure, which varies in time (cf. lower row of Fig. 5). These structures are caused by dust layers in the outer parts of the shell which, due to the deviations from strict temporal periodicity of the dust formation process, do not form a spatial pattern as regular as is the case in Models A and B.

During the dust formation cycle shown in Fig. 5 (between $0.0P$ and $3P$), the visibilities at $q = 10^6\,\mathrm{rad}^{-1}$ vary by 21% at 1.65μm, by 35% at 5μm, and by 78% at 12μm. The minimum of the 1.65μm and 5μm visibility is reached at $t = 0.45P$ and $t = 0.50P$, respectively, while the minimum visibility for 12μm is reached at $t = 2.00P$. The maximum values occur for 1.65μm and 5μm at $t = 2.80P$ and $t = 2.90P$, respectively and for 12μm at $t = 0.90P$.

Thus, the visibilities at $q = 10^6\,\mathrm{rad}^{-1}$ would indicate a maximum extension of the regions radiating at 1.65μm and 5μm around phase $0.50P$, shortly before a second shock will lead to subsequent growth of the dust particles already contained in the innermost dust layer (cf. Fig. 2). The maximum extension derived from the visibility at 12μm appears at the instant of complete condensation in the innermost dust layer.

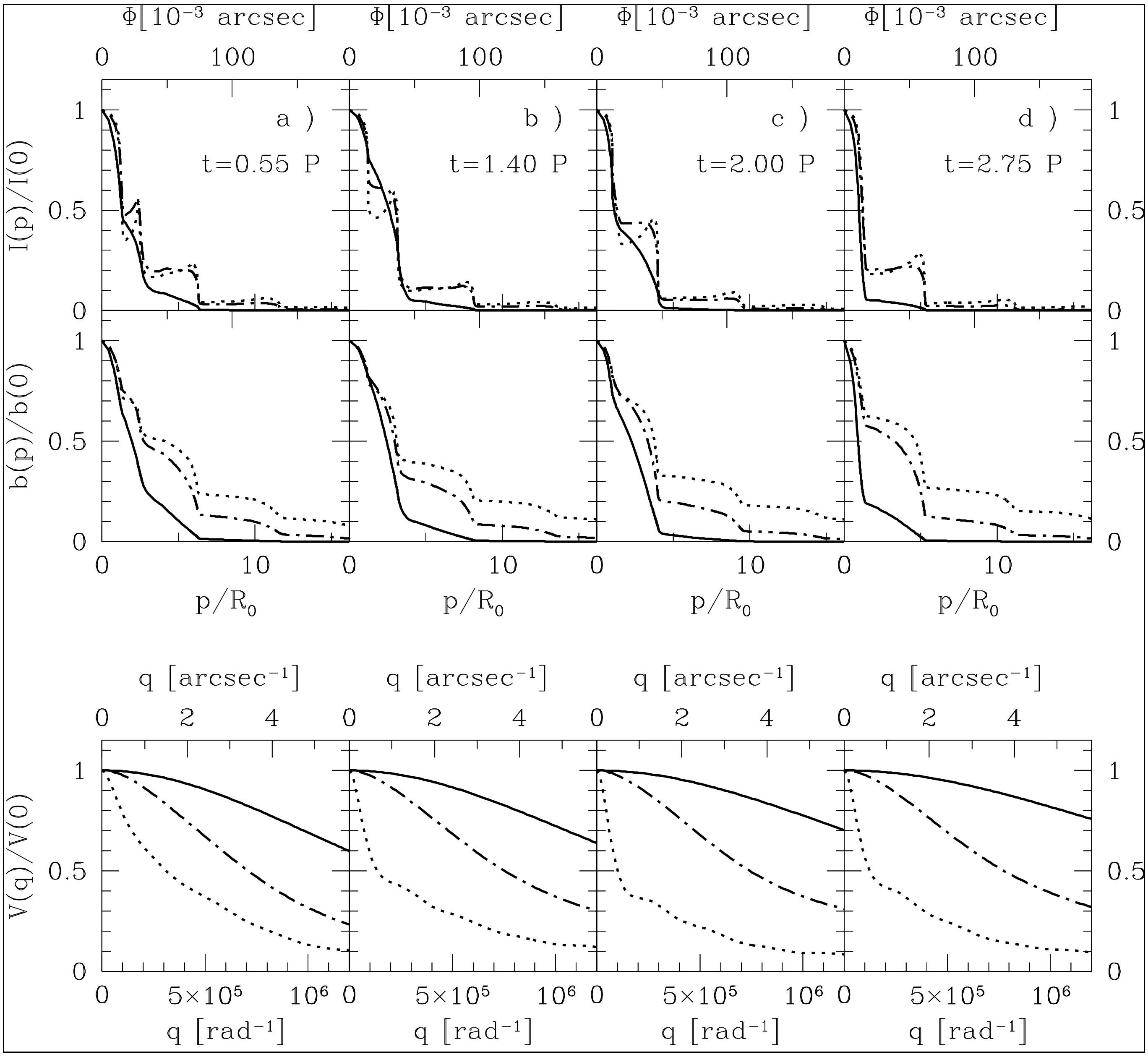

Fig. 5. Same as Fig. 3, but for Model C

Minimum extension, on the other hand, occurs for the two shorter wavelengths at a phase around minimum optical depth, when the next dust layer starts to form. At 12μm, the instant of minimum extension appears during a phase of increasing optical depth, caused by subsequent growth of grains in the innermost dust layer.

3.3.4. Summary of results

In Tab. 2 the results described in the previous paragraphs concerning maximum and minimum extension of the models A, B, and C are summarized. Maximum visibility at the two shorter wavelengths generally occurs shortly *after* the instant of minimum optical depth, during the phase of effective dust condensation in the new layer. These instants of time correspond for all models to the decreasing branches of the lightcurves, shortly before the (deep) light minima are reached (cf. Fig. 2). At longer wavelengths (e.g. $\lambda = 12\mu$m), maximum visibility is reached during phases, which are dominated by expansion of all the layers present in the CDS. The instants of minimum visibility, as is expected, occur during phases, when the layers have considerably moved outwards. An exception is found for Model B, where already a new dust layer starts to form, when minimum visibility is reached at 5μm and 12μm. At this instant, however, the forming layer is

Table 2. Emitting regions of models A, B, and C at the instants of minimum and maximum visibilities at $q = 10^6\,\mathrm{rad}^{-1}$ for different wavelengths. The 3rd. column gives the relative variation of the visibility during the dust formation cycle. $t_{\min}$ and $t_{\max}$ denote the instants of time, when minimum and maximum visibility is reached, respectively. The last column gives the instant of time, when minimum optical depth is reached, i.e. the instant just prior to the formation of a new dust layer. Phases correspond to those plotted in Fig. 2.

Mod.	λ [μm]	relative var. [%]	$t_{\min}$ [P]	major contributions to $I(p)$ from	$t_{\max}$ [P]	major contributions to $I(p)$ from	$t(\tau_{\min})$ [P]
A	1.65	12	0.45	1st. layer	0.65	stellar surface	0.60
	5	30	0.40	1st. + 2nd. layer	0.75	1st. + 2nd. layer	
	12	66	0.40	1st. + 2nd. layer	1.00	1st. + 2nd. layer	
B	1.65	38	1.25	1st + 2nd. layer	3.25	stellar surface	3.20
	5	34	3.35	(forming) + 1st. + 2nd. layer	0.45	1st., 2nd. + 3rd. layer	
	12	68	3.35	(forming) + 1st. + 2nd. layer	1.50	1st., 2nd. + 3rd. layer	
C	1.65	21	0.45	1st. + 2nd. layer	2.80	stellar surface	2.75
	5	35	0.50	1st. + 2nd. layer	2.90	1st. + 2nd. layer	
	12	78	2.00	1st. + 2nd. layer	0.90	1st. + 2nd. layer	

only seen as slight peak on the dominating broad structure produced by the layer originating from the previous dust formation cycle (cf. upper diagram in Fig. 4c)).

From the general course of the visibility functions at different wavelengths, a clear trend is apparent for all three models, in the sense of increasing angular size of the shells with increasing wavelength (cf. Figs. 3, 4, and 5). This trend reverses towards even longer wavelengths, since due to the decreasing optical depths at longer wavelengths and thus decreasing contribution of thermally emitted radiation, the dust layers again appear less pronounced in the intensity profiles.

4. Discussion and comparison with observations

Temporal variations of observed visibility functions have frequently been reported in the literature (e.g. McCarthy et al. 1980, Ridgway & Keady 1988, Dyck et al. 1991, Danchi et al. 1990, 1994). For example, McCarthy et al. (1980) found an increase of the measured 5μm visibility by 30% between maximum and minimum phase of the lightcurve in the case of IRC +10216. This magnitude of variation is in excellent agreement with the variation of the 5μm visibilities resulting from the three models presented in Sect. 3.3. These temporal changes usually are interpreted by means of a periodic variation of the inner dust shell boundary. In particular, from such observations the conclusion was drawn, that dust formation takes place close to the phase of light minimum (cf. Danchi et al. 1990, 1994) which is confirmed by our model calculations. Structural changes of IRC +10216 on a time scale of one year were also noted by Ridgway & Keady (1988), who interpreted this fact by means of dust destruction near maximum light. At $\lambda = 11\mu$m, Danchi et al. (1990) found substantial temporal variations of the IRC +10216 visibility ($\approx 50\%$ at a spatial frequency $q = 3\,10^5\,\mathrm{rad}^{-1}$) and interpreted this result by the formation of new dust near minimum luminosity. In a recent investigation, Danchi et al. (1994) present visibility measurements for 13 late–type stars in the 11μm region obtained over a time interval of five years. They find substantial variations of the visibilities with time for many of these stars and interpret this result by periodic dust formation near the phase of light minimum. For the oxygen–rich star Mira (*o* Ceti) they find in particular, that the visibilities vary from cycle to cycle enough to give notable differences at the same *phase* of the lightcurve but in different cycles, i.e. the visibility (and thus the spatial structure) is not repeating from cycle to cycle. Such a behaviour results as a natural consequence from the multiperiodic Models B and C (cf. e.g. Fig. 4b) and c)). In order to confirm the mechanism of the formation of new dust layers on timescales different from the pulsation period of the star as being responsible for these latter temporal changes in the observed spatial spectra, it would be very valuable to obtain time series of spatial spectra in particular for the promising C–stars. These objects could be selected by means of their multiperiodic lightcurves (e.g. R For, R Scl, AFGL 935, AFGL 3099 (Le Bertre 1992), or AFGL 3068 (Le Bertre et al. 1995)). As is demonstrated in Paper II, such lightcurves are produced by our models in a rather natural way by the multiperiodic formation of new discrete dust layers.

Internal structures in the spatial spectra have been observed in C–rich objects (e.g. CIT 5, CIT 6 (Dyck et al. 1984); IRC +10216 (Sutton et al. 1979, Ridgway & Keady 1988, Danchi et al. 1994) as well as in O–rich objects (e.g. VY CMa, NML Cyg (Dyck et al. 1984); *o* Ceti, α Ori, NML Tau (Danchi et al. 1994)), which cannot be accounted for by a continuous intensity profile resulting from the usually assumed power–law dust distribution. Therefore, multicomponent models were proposed for describing the radial dust distribution in these cases (e.g. Toombs et al. 1972, Dyck et al. 1984, Danchi et al. 1994).

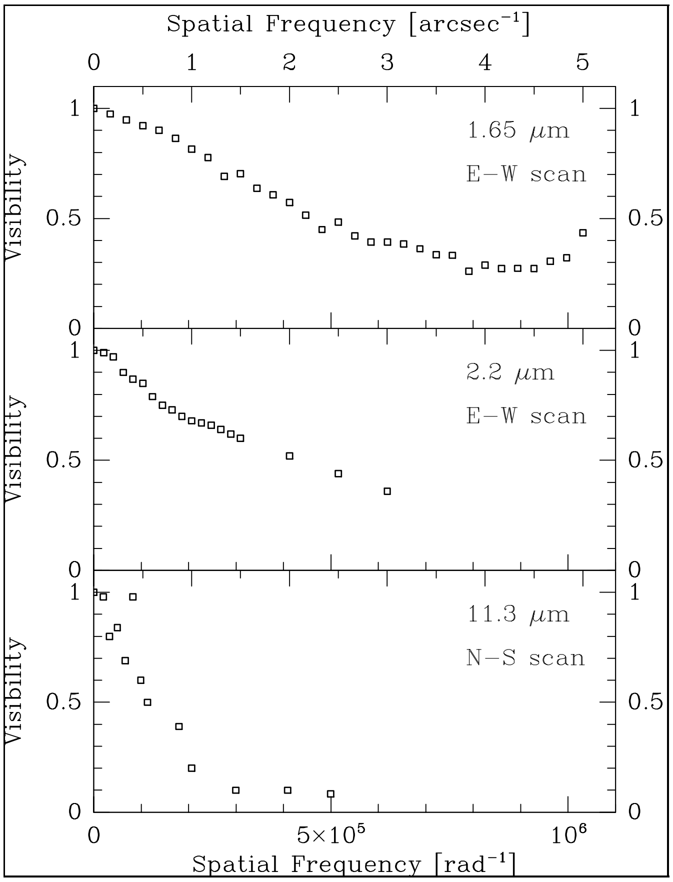

Fig. 6. Observed visibilities of IRC +10216 at different wavelengths after Ridgway & Keady (1988). The data were kindly provided by Dr. J. J. Keady (1994, private communication).

In the models presented here, small scale structures are produced in the synthetic visibility functions at longer wavelengths ($\lambda > 10\mu$m) by the pronounced step–like intensity distribution, which is a natural consequence of the layered dust distribution resulting from our model calculations.

A pronounced rippled structure in the visibilities of IRC +10216 is evident at 1.65μm, 2.2μm, 3.15μm and in the 10μm region (cf. Ridgway & Keady 1988, and Fig. 6). Ridgway & Keady (1988) performed a one–dimensional image reconstruction of the measured visibilities and, additionally, of a lunar occultation measurement obtained at 4.65μm, which all yield obvious step–like structures in the images (i.e. the intensity profiles) on a typical scale of approximately 0.1 arcsec. However, no reliable physical model has been proposed so far which could explain these observed structures.

From Fig. 6 also a substantial wavelength dependence of the apparent extension of the dust shell around IRC +10216 is evident. This behaviour has also been found e.g. by Dyck et al. (1984) for several other objects. They performed speckle interferometry in the near–infrared spectral region between 1.65μm and 4.8μm for 16 late–type stars and bipolar nebulae. To interpret the observations, Dyck et al. (1984) assumed the visibility functions to be Gaussian distributions and fitted the FWHM (full width at half maximum) θ for the different objects. They found, that θ varies as λ^α in the observed wavelength range, with $\alpha \approx 0.2$ in the case of C–stars and $0.7 < \alpha < 1.3$ in the case of M–stars, indicating different dust opacities for both types of objects. They also noted as a further general trend, that the objects with higher mass loss rates have significantly larger angular diameters than those with smaller rates. Both facts are also evident from the calculations presented here (cf. Figs. 3, 4, and 5). In our models, the wavelength dependence of the apparent extension is largely caused by the increasing contributions emanating from the outer dust layers for increasing wavelengths in the near– and mid–infrared region. The increasing apparent diameter with increasing mass loss rate is caused by the larger amount of thermally emitting dust along the line of sight in the models with higher mass loss rates.

Recently, Richichi et al. (1993, private communication) obtained a lunar occultation lightcurve of IRC +10216 at $\lambda = 1.65\mu$m, which gives a one–dimensional radial brightness profile with an angular resolution of 0.002 arcsec. The algorithm used for the image reconstruction from the occultation lightcurve is described in Richichi (1989) and already has been successfully applied to several late–type stars (Richichi 1989, Richichi et al. 1991, Richichi et al. 1995).

In the reconstructed image of IRC +10216, a quite regular step–like structure on an angular scale of about 0.03 arcsec is evident to the right of the central peak. If the FWHM of the central peak ($\Phi \approx 45$ milli–arcsec (mas)) is conceived as the stellar diameter (i.e. $R_\star \mathrel{\hat{=}} \Phi/2$), then the separation of the first three steps from the center of the peak ($\approx$ 31.4 mas, 57 mas, and 86 mas) correspond to a radial distance of $1.4R_\star$, $2.5R_\star$, and $3.8R_\star$ from the center of the star.

A quantitative comparison between different observations and the results of a time–dependent model calculation will be presented in collaboration with Dr. A. Richichi in a separate paper, entirely devoted to IRC +10216. There, a detailed comparison between observed and calculated brightness profiles, spatial spectra, spectral energy distribution, and lightcurves will be given.

At the present state, however, it is not yet intended to describe any real object by one of the Models A–C discussed here. Nevertheless, in order to allow for a qualitative comparison with the lunar occultation observation, the locations of the intensity steps of Model A (cf. Fig. 3), whose period is close to that of IRC +10216, are given below. The first three steps (corresponding to the three innermost dust layers) in the **synthetic** images are located at

$t = 0.25P$: $1.4R_0$, $3.6R_0$, $7.9R_0$
$t = 0.60P$: $1.6R_0$, $5.1R_0$, $9.6R_0$
$t = 0.75P$: $1.5R_0$, $2.7R_0$, $5.7R_0$

$t = 1.00P$: $1.2R_0$, $3.0R_0$, $6.8R_0$
while the **observation** shows steps at
$1.4R_\star$, $2.5R_\star$, $3.8R_\star$
These numbers are independent of the assumed distance to IRC +10216, which is still a matter of debate and might be as low as 100pc (e.g. Becklin et al. 1969 or as large as 300pc (e.g. Herbig & Zappala 1970)). From the numbers given above, it is evident that the separation between the steps in the synthetic images of Model A is somewhat larger than it is the case for IRC +10216. The deviation increases with increasing distance of the dust layers from the center of the star. However, this behaviour can easily be understood since the velocity in Model A has already reached a value around $20\,\mathrm{kms}^{-1}$ at $5R_0$ (cf. Fig. 1), whereas the *terminal* outflow velocity of IRC +10216 is considerably smaller ($v_\infty \approx 15\,\mathrm{kms}^{-1}$, e.g. Olofsson et al. (1993a)) and is reached only around $20R_\star$ (cf. Keady & Ridgway 1993). The dust layers produced in the model calculation, therefore, move much faster outwards than does the material in the inner shell region of IRC +10216. The steep increase of the calculated velocity field causes the rapidly increasing separation between successive layers with increasing distance from the star. Nevertheless, the location of the steps resulting from the model calculation agrees within a factor of 2–3 with the location of the structures in the observed intensity profile, which is of the same order as is the expected velocity difference between model and object in the inner shell region. This satisfactory agreement between the results of the model calculation and the observed structure of IRC +10216 strongly suggests that the formation of discrete dust layers is not only a theoretical result, but also a real phenomenon, actually occurring in the circumstellar shells of pulsating late–type stars.

One major problem concerning the comparison between synthetic and observed image however, remains to be resolved: The image of IRC +10216 exhibits the pronounced step–like structure already at a wavelength of $\lambda = 1.65\mu$m, whereas the model calculation produces this significant intensity distribution only at wavelengths $\lambda > 3\mu$m. Also, in the synthetic visibilities internal structures are only present at wavelengths larger than approximately 10μm, while the observed visibilities exhibit such structures already at 1.65μm (cf. Fig. 6). The strength of the structures in the synthetic brightness profiles depends on the wavelength via the transport coefficients of the dust grains. Thus, the wavelength–dependence of the dust opacity is crucial for a quantitative modelling of the intensity profiles and spatial spectra of the real objects. However, there exist up to now no unique information about the optical properties of the grains formed in real carbon–rich circumstellar environments. Several optical constants appropriate for amorphous carbon are available from the literature (e.g. Maron (1990), Rouleau & Martin (1991), Preibisch et al. (1993)) which, however, result in different wavelength dependences of the calculated transport coefficients. Recent work on the spectral modelling of individual C–stars (e.g. Jura (1983), Le Bertre (1987, 1988b, 1988a)) suggests a $\lambda^{-1.3}$ dependence of the dust opacity, while the Maron (1990) data used in the present work give roughly a λ^{-1} dependence. A first problem with respect to the opacity law was already encountered in the lightcurves of Model A (cf. Paper II), which show the shallow intermediate maxima on the ascending branch only at longer wavelengths than it is observed. Secondly, from the near–infrared colours of our models a small, but systematic deviation with respect to the observations was found and attributed to the smooth wavelength–dependence of the dust absorption efficiency used in the present model calculations (Winters 1994). All these problems mentioned might be resolved simultaneously, if the dust grains formed in the shells of the real objects are indeed characterized by an internal structure intermediate between the pure amorphous (i.e. $\kappa \sim \lambda^{-1}$) and the pure crystalline (i.e. $\kappa \sim \lambda^{-2}$) modification. This would produce a steeper opacity law than it is used here and in principle would lead to smaller optical depths at near–infrared wavelengths. Since a different opacity law however, would also influence the details of the dynamic model structure, which is the result of a strongly nonlinear problem, a definite answer cannot be given at the present state.

5. Conclusions

Theoretical brightness distributions and visibilities of carbon–rich long–period variables are presented.

Based on dynamical models of CDS, which include time–dependent hydrodynamics and a detailed treatment of the processes of formation, growth and evaporation of carbon grains, frequency–dependent radiative transfer calculations have been carried out which yield the synthetic brightness distributions and visibilities of these dust shell models.

The calculations discussed in this paper are not designed to describe any individual object but to investigate the basic physical mechanisms occurring in a pulsating dust forming atmosphere and to derive general observable consequences.

It is shown that the characteristic discrete shell–like distribution of the dust resulting from these models causes significant structures in the surface brightness distributions and in the synthetic visibility functions, which are in qualitative agreement with lunar occultation observations and interferometric measurements of circumstellar dust shells around carbon–rich LPVs. We also find temporal variations of the synthetic spatial spectra, which are in quantitative agreement with respective observations. Additionally, the results of our calculations indicate, that the instants of time, when the maximum and minimum value of the visibility is reached, depend on wavelength.

The comparison between the theoretical results and the observations shows that already our rather simple coupling of the dynamic dust shell calculations and the radiative transfer calculations is a promising approach to understand the optical appearance of carbon–rich LPVs.

Acknowledgements. The authors thank the referee, Dr. Thibaut Le Bertre, for his valuable suggestions. We are grateful to Dr. Andrea Richichi for making available to us his plot of the intensity profile of IRC +10216 prior to publication. Thanks are also due to Beate Patzer for useful comments and discussions. J.M.W. acknowledges financial support by the *Arbeitsamt V, Berlin* during the period of time when this paper was written. The calculations were performed on the CRAY computers of the Konrad–Zuse–Zentrum für Informationstechnik Berlin and the HLRZ, Jülich. Subsequent data analysis has been performed on the WAP–cluster of the physics department of the TU Berlin. This work has been partly supported by the Deutsche Forschungsgemeinschaft, *DFG*–Schwerpunkt "Theorie kosmischer Plasmen" (grant Se 420/5–4). Part of this research was performed under the auspices of the U.S. Department of Energy.

References

Allen C. W., 1973, Astrophysical Quantities. The Athlone Press, London
Becklin E. E., Frogel J. A., Hyland A. R., Kristian J., Neugebauer G., 1969, ApJ 158, L133
Boothroyd A. I., Sackmann I.-J., 1988, ApJ 328, 641
Bowen G. H., 1988, ApJ 329, 299
Bowen G. H., 1990, Dynamical phenomena in pulsating star atmospheres. In: Buchler J. R. (ed.) The Numerical Modelling of Nonlinear Stellar Pulsations. Kluwer Academic Publishers, p. 155
Bracewell R. N., 1965, The Fourier Transform and its Applications. McGraw–Hill, New York
Claussen M. J., Kleinmann S. G., Joyce R. R., Jura M., 1987, ApJS 65, 385
Danchi W. C., Bester M., Degiacomi C. G., McCullogh P. R., Townes C. H., 1990, ApJ 359, L59
Danchi W. C., Bester M., Degiacomi C. G., Greenhill L. J., Townes C. H., 1994, AJ 107, 1469
Dyck H. M., Zuckerman B., Leinert C., Beckwith S., 1984, ApJ 287, 801
Dyck H. M., Benson J. A., Howell R. R., Joyce R. R., Leinert C., 1991, AJ 102, 200
Feuchtinger M. U., Dorfi E. A., Höfner S., 1993, A&A 273, 513
Fleischer A. J., 1994, PhD thesis, Technische Universität, Berlin, FRG
Fleischer A. J., Gauger A., Sedlmayr E., 1992, A&A 266, 321 (Paper I)
Fleischer A. J., Gauger A., Sedlmayr E., 1995, A&A in press
Frantsman Y. L., Eglitis I. E., 1988, SvA 14, L109
Gail H.-P., Keller R., Sedlmayr E., 1984, A&A 133, 320
Gail H.-P., Sedlmayr E., 1987, A&A 171, 197
Gail H.-P., Sedlmayr E., 1988, A&A 206, 153
Gauger A., Gail H.-P., Sedlmayr E., 1990, A&A 235, 345
Gauger A., Fleischer A. J., Winters J. M., Sedlmayr E., 1994, Circumstellar shells of long–period variables: Dust formation and optical appearance. In: Clegg R. E. S., Meikle P., Stevens I. (eds.) Circumstellar Media in the late stages of Stellar evolution. Cambridge University Press, Cambridge
Herbig G. H., Zappala R. R., 1970, ApJ 162, L15
Höfner S., Feuchtinger M. U., Dorfi E. A., 1995, A&A in press
Holzer T. E., Flå T., Leer E., 1983, ApJ 275, 808
Jones T. W., Ney E. P., Stein W. A., 1981, ApJ 250, 324
Jura M., 1983, ApJ 267, 647
Jura M., 1986, Ir. Astron. J. 17, 322
Keady J. J., Ridgway S. T., 1993, ApJ 406, 199
Krüger D., Gauger A., Sedlmayr E., 1994, A&A 290, 573
Lambert D., Gustafsson B., Eriksson K., Hinkle K. H., 1986, ApJS 62, 373
Le Bertre T., 1987, A&A 176, 107
Le Bertre T., 1988a, A&A 190, 79
Le Bertre T., 1988b, A&A 203, 85
Le Bertre T., 1992, A&AS 94, 377
Le Bertre T., Gougeon S., Le Sidaner P., 1995, A&A in press
Loup C., Forveille T., Omont A., Paul J. F., 1993, A&AS 99, 291
Lucy L. B., 1971, ApJ 163, 95
Lucy L. B., 1976, ApJ 205, 482
MacGregor K. B., Stencel R. E., 1992, ApJ 397, 644
Maron N., 1990, Ap&SS 172, 21
Martin P. G., Rogers C., 1987, ApJ 322, 374
McCarthy D. W., Howell R., Low F. J., 1980, ApJ 235, L27
Nather R. E., McCants M. M., 1970, AJ 75, 963
Olofsson H., Eriksson K., Gustafsson B., Carlström U., 1993a, ApJS 87, 267
Olofsson H., Eriksson K., Gustafsson B., Carlström U., 1993b, ApJS 87, 305
Pijpers F. P., Habing H. J., 1989, A&A 215, 334
Preibisch T., Ossenkopf V., Yorke H. W., Henning T., 1993, A&A 279, 577
Richichi A., 1989, A&A 226, 366
Richichi A., Lisi F., Calamai G., 1991, A&A 241, 131
Richichi A., Chandrasekhar T., Lisi F., et al., 1995, A&A in press
Richtmyer R. D., Morton K. W., 1967, Difference methods for initial-value problems. John Wiley & Sons, New York, 2^{nd} edition
Ridgway S. T., Keady J. J., 1988, ApJ 326, 843
Rouleau F., Martin P. G., 1991, ApJ 377, 526
Rowan-Robinson M., Harris S., 1983, MNRAS 202, 797
Sutton E. C., Betz A. L., Storey J. W. V., Spears D. L., 1979, ApJ 230, L105
Tielens A. G. G. M., 1983, ApJ 271, 702
Toombs R. I., Becklin E. E., Frogel J. A., et al., 1972, ApJ 173, L71
Williams J. D., 1939, ApJ 89, 467
Willson L. A., Struck-Marcell C., Bowen G., 1994, Winds from pulsating stars. In: Jokipii J. R., Sonett C. P., Giampapa M. S. (eds.) Cosmic Winds and the Heliosphere. University of Arizona Press, Tucson (in press)
Winters J. M., 1994, PhD thesis, Technische Universität, Berlin, FRG
Winters J. M., Dominik C., Sedlmayr E., 1994a, A&A 288, 255
Winters J. M., Fleischer A. J., Gauger A., Sedlmayr E., 1994b, A&A 290, 623 (Paper II)
Winters J. M., Fleischer A. J., Sedlmayr E., Gauger A., 1995, Ap&SS in press
Wood P. R., 1979, ApJ 227, 220

This article was processed by the author using Springer-Verlag LaTeX A&A style file *L-AA* version 3.